



THE UNIVERSITY *of* EDINBURGH

## Edinburgh Research Explorer

### 3D plane labeling stereo matching with content aware adaptive windows

**Citation for published version:**

Horna carranza, L & Fisher, R 2017, 3D plane labeling stereo matching with content aware adaptive windows. in *Proceedings of the 12th International Joint Conference on Computer Vision, Imaging and Computer Graphics Theory and Applications*. SCITEPRESS, pp. 162-171, 12th International Joint Conference on Computer Vision, Imaging and Computer Graphics Theory and Applications, Porto, Portugal, 27/02/17. <https://doi.org/10.5220/0006105401620171>

**Digital Object Identifier (DOI):**

[10.5220/0006105401620171](https://doi.org/10.5220/0006105401620171)

**Link:**

[Link to publication record in Edinburgh Research Explorer](#)

**Document Version:**

Peer reviewed version

**Published In:**

Proceedings of the 12th International Joint Conference on Computer Vision, Imaging and Computer Graphics Theory and Applications

**General rights**

Copyright for the publications made accessible via the Edinburgh Research Explorer is retained by the author(s) and / or other copyright owners and it is a condition of accessing these publications that users recognise and abide by the legal requirements associated with these rights.

**Take down policy**

The University of Edinburgh has made every reasonable effort to ensure that Edinburgh Research Explorer content complies with UK legislation. If you believe that the public display of this file breaches copyright please contact [openaccess@ed.ac.uk](mailto:openaccess@ed.ac.uk) providing details, and we will remove access to the work immediately and investigate your claim.



# 3D plane labeling stereo matching with content aware adaptive windows

Luis Horna<sup>1</sup>, and Robert B. Fisher<sup>1</sup>

<sup>1</sup>IPAB, The University of Edinburgh, Edinburgh, UK  
s1145121@sms.ed.ac.uk, rbf@inf.ed.ac.uk

Keywords: Stereo matching, 3D labeling, adaptive windows.

Abstract: In this paper, we present an algorithm that exploits both the underlying 3D structure and image entropy to generate an adaptive matching window. The presented algorithm estimates real valued disparity maps by smartly exploring a 3D search space using a novel hypothesis generation approach that acts like a propagation scheduler. The proposed approach is among the top performing results when evaluated in the Middlebury, KITTI 2015 benchmarks.

## 1 INTRODUCTION

The problem of 3D plane labeling to estimate depth from two or more images has become the focus area of modern stereo matching algorithms. The core issue in 3D plane labeling using two images (left  $I_l$  and right  $I_r$  views of a scene) is finding the correspondences for each pixel from image  $I_l$  to  $I_r$  by assigning a 3D plane that produces a real valued disparity<sup>1</sup>. This process is better modeled as an optimization problem where the objective is to compute the disparity assignment that minimizes eq.1.

$$E(D) = \arg \min_D \sum_p^{NumP} \{C_p(D_p) + \sum_{q \in N(p)} V_{pq}(D_p, D_q)\} \quad (1)$$

$E(D)$  is the cost of the disparity assignment (energy),  $D$  is a set of planes and  $D_p$  encodes a plane at pixel  $p$ , that gives the disparity of the pixel at  $p$  with respect to another image.  $D_p(q)$  is the disparity estimated using plane  $D_p$  evaluated at pixel  $q$ . The plane  $D_p$  has two parameters: a 3D unit normal vector  $\hat{n}_p = (n_p^x, n_p^y, n_p^z)$  and disparity  $d_p$ . The disparity of pixel  $q = (x_q, y_q)$  using  $D_p$  is given by:

$$D_p(q) = a * x_q + b * y_q + c \quad (2)$$

where  $a = -\hat{n}_p^x / \hat{n}_p^z$ ,  $b = -\hat{n}_p^y / \hat{n}_p^z$  and  $c = (\hat{n}_p^x * x_q + \hat{n}_p^y * y_q + \hat{n}_p^z * d_p) / \hat{n}_p^z$  as in (Bleyer et al., 2011).  $C_p$  is a function that measures the similarity/dissimilarity of two pixels (e.g.  $I_l(p)$  and  $I_r(p + D_p(p))$ ), and  $NumP$  is the number of pixels in the image.  $N(p)$

is a neighborhood around  $p$ , and  $q$  is a neighbor of  $p$ .  $V_{pq}$  (smoothness term) is a function that evaluates how well the disparity at position  $p$  fits its neighbors. Eq.1 is typically represented as Markov Random Field (MRF) and minimized using either Graph Cuts (GC), Loopy Belief Propagation (LBP) or Tree Re-weighted with Sequential (TRW-S) update. In this paper inference/minimization is done using TRW-S (Kolmogorov, 2007).

In this paper, we present an algorithm that exploits the underlying 3D structure, image texture to generate an adaptive matching window, and a 3D search using a novel hypothesis generation approach to estimate real valued disparity maps.

## 2 RELATED WORK

The idea of assigning planes per pixel to estimate sub-pixel disparity has been previously used in (Klaus et al., 2006; Woodford et al., 2007; Bleyer et al., 2011; Besse et al., 2012; Olsson et al., 2013; Heise et al., 2013; Taniai et al., 2014; Sinha et al., 2014; Yamaguchi et al., 2014). These algorithms can be classified in two categories: fixed plane inference (FPI) and dynamic plane inference (DPI). FPI algorithms make an initial disparity estimation and then extract the planes, which are then used during the inference process to estimate disparity. By contrast DPI algorithms assign one or more planes to each pixel, and then propagate “good” planes (i.e. low/high scores depending on the cost function) to neighbors/regions under the assumption that neighbors/regions are likely to have the same plane. Then in a refinement stage the

<sup>1</sup>The displacement along a search area is known as disparity.

planes are improved, thus the planes are dynamically updated. DPI algorithms in particular have become the state of the art (e.g. (Bleyer et al., 2011; Besse et al., 2012; Heise et al., 2013; Taniai et al., 2014)).

Common issues in DPI algorithms include the use of large adaptive windows (commonly using (Yoon and Kweon, 2006)) or segment (Li et al., 2015) based similarity cost to compute the similarity/dissimilarity cost, which can result in a strong bias towards large planes. A possible solution to this issue is to change the window size, which requires either some assumption about the 3D structure or image content. However, changing the window size can result in poor performance in textureless areas and thus requires additional assumptions such as the uniqueness constraint or occlusion penalties. Another issue in DPI algorithms such as (Bleyer et al., 2011; Besse et al., 2012) is that the hypothesis generation and propagation is done sequentially.

## 2.1 Contributions

To address some of the issues described the proposed approach makes the following contributions:

- Content aware adaptive window aggregation: Reduces error and loss of details.
- Use of a cost function that imposes a local hypothesis uniqueness, unlike (Klaus et al., 2006; Woodford et al., 2007; Olsson et al., 2013; Yamaguchi et al., 2014; Sinha et al., 2014; Bleyer et al., 2011; Besse et al., 2012; Taniai et al., 2014): Helps to handle textureless surfaces, and does not required higher order interactions (unlike (Vogel et al., 2015)) in a MRF.
- Use of a cost function that penalizes disparity values outside a defined search range: Prevents invalid disparity values assignment.
- Use of a single global hypothesis per disparity plane: Eliminates the need to update multiple hypotheses.
- Use of a hypothesis generator that acts as a propagation scheduler: Helps to do a search in a 3D space.

## 3 PROPOSED ALGORITHM

The proposed approach to estimate a 3D plane labeling per pixel has the following components:

- Content aware slanted windows to compute the data term (pixel similarity measure).
- Uniqueness and out of range terms.
- Adaptive search range.

- Smoothness term that adapts to image content.
- Hypothesis generation/update that acts as a propagation scheduler.

The novel content aware windows exploit both intensity and 3D structure (if available) to adapt the window size and similarity function. It's important to note that the proposed hypothesis generation provides an alternative to sequential algorithms (e.g. (Bleyer et al., 2011; Besse et al., 2012)) and does not impose restrictions to the pairwise interactions like (Taniai et al., 2014).

### 3.1 Content aware adaptive similarity function

DPI algorithms commonly use the adaptive window (eq.4) from (Yoon and Kweon, 2006), which has the following issues: bias towards large planes (good quality in textureless areas), center pixel bias for large windows (results in loss of detail, e.g. fig.1), and noisy results for small windows. The center pixel bias can be reduced by using the windows from (Zhang et al., 2009), which adapts better to local image changes, but can give poor results if the windows are poorly estimated or window size is not large (particularly in textureless areas). To compensate for the center pixel bias while keeping good performance in textureless areas, a texture measure  $L_p$  (eq.3) is used to balance the influence of eq.4 and eq.5 (fixed size modified version of (Zhang et al., 2009)) in eq.7.

$$L_p = \left\{ e^{-\frac{T_p}{T_w}} \left| T_p = \frac{1}{Z} \sum_{q \in N(p)} e^{-\frac{|I_p - I_q|}{\sigma_r}} h(p) \right. \right\} \quad (3)$$

$$AW_p(D_p) = \frac{1}{Z} \sum_{q \in N(p)} e^{-\frac{|I_p - I_q|}{\sigma_r}} c_q(D_p) \quad (4)$$

$$CW_p(D_p) = \frac{1}{Z_v} \sum_{q \in N_v(p)} e^{-\frac{|I_p - I_q|}{\sigma_r}} CW_q^h(D_p) \quad (5)$$

$$CW_q^h(D_p) = \frac{1}{Z_h} \sum_{s \in N_h(q)} e^{-\frac{|I_s - I_q|}{\sigma_r}} c_s(D_p) \quad (6)$$

$$C_p(D_p) = L_p \cdot AW_p(D_p) + (1 - L_p) \cdot CW_p(D_p) \quad (7)$$

where  $Z$ ,  $Z_h$ ,  $Z_v$  are normalization constants such that the weights in the neighbourhood add up to one,  $h(p)$  is a  $5 \times 5$  entropy filter,  $|I_p - I_q|$  is the  $L1$  distance in  $RGB$  space,  $N(p)$  is the neighborhood around  $p$  ( $n \times n$  window),  $N_h(p)$  and  $N_v(q)$  are the horizontal ( $1 \times n$ ) and vertical ( $n \times 1$ ) neighborhoods around  $p$  and  $q$ . Eq.3 is the adaptively filtered version of  $h(p)$ , which is done to clean the noisy measure, and better balance  $AW_p$  and  $CW_p$  close to edges.

The adaptive window from (Zhang et al., 2009) was modified as follows: Use of range terms for vertical and horizontal directions. Only horizontal arms are computed, while the vertical arm remains of a

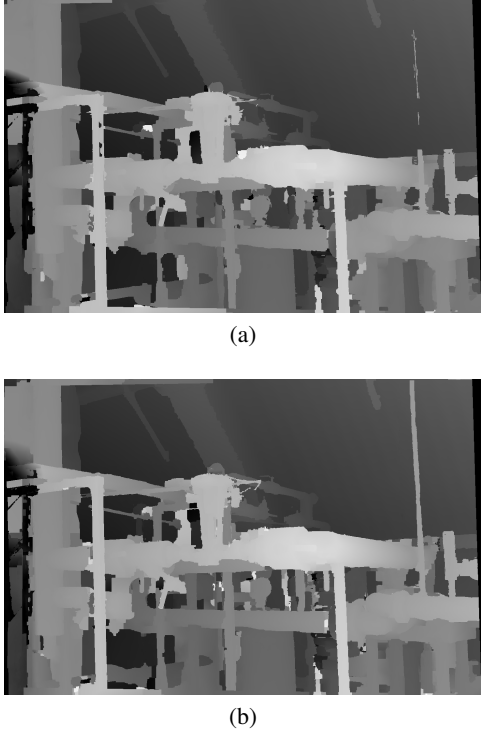


Figure 1: Raw result of Pipes image with AW(a) and AW + CW(b) functions. Parameters used as in sec.6.

fixed size. The pixel similarity function is given by:

$$c_p(D_p) = \alpha c_p^1(D_p(p)) + c_p^2(D_p(p)) \quad (8)$$

$$c_p^1(D_p) = \min(|\nabla I_p^1 - \nabla I_{p+D_p}^2|, \tau_{grad}) \quad (9)$$

$$c_p^2(D_p) = \min(\chi(I^1, I^2, p, D_p), \tau_{cen}) \quad (10)$$

where,  $I^1$  is the reference image, and  $I^2$  is the target image,  $c_p^1(D_p)$  is the truncated absolute differences of gradients,  $c_p^2(D_p)$  is the Truncated Hamming distance of census transform (Zabih and Li, 1994),  $\chi$  computes the census transform at  $p$  and displacement  $D_p$  and Hamming distance,  $\alpha$  balances the pixel-wise cost influence. Note that  $D_p(p)$  is the disparity resulting from the evaluation of plane  $D_p$  at pixel  $p$ .

The adaptive window described so far works under the assumption that the window size remains constant all over the image, which can lead to either loss of detail<sup>2</sup> (large windows), noisy results (small windows), and bias towards large planes. To reduce these effects the window size is selected based on a local measure  $W_p$ , which describes the behavior of an initial disparity map gradient around a region. A region is a superpixel segment obtained using SLIC (Achanta et al., 2012). The behavior of the initial disparity

<sup>2</sup>In particular adaptive windows have a tendency to lose thin vertical details.

map gradient is first measured along the pixels in the segment perimeter (eq.11), then a segment difference measure is computed using the median disparity of neighbouring segments (eq.12), and later propagated per pixel (eq.13) to reduce the effect of noise from the initial disparity map. Thus window size at each pixel  $p$  is computed using  $n = \Omega(p)$  in eq.14.

$$\hat{w}_p = \frac{1}{K|\hat{N}(p)|} \sum_{q \in \hat{N}(p)} \left[ |\tilde{d}_p - \tilde{d}_q| \geq \frac{2}{5} K_w \right] \quad (11)$$

$$w_p = \begin{cases} \frac{1}{K|\hat{N}(p)|} \sum_{q \in \hat{N}(p)} \min(|\tilde{d}_p - \tilde{d}_q|, K_w) & : \hat{w}_p > \tau_w \\ 0 & : \text{otherwise} \end{cases} \quad (12)$$

$$W_p = \left\{ \frac{1}{Z} \sum_{q \in \hat{N}(p)} e^{-\frac{|I_p - I_q|}{\sigma_r}} w_p \mid Z = \sum_{q \in \hat{N}(p)} e^{-\frac{|I_p - I_q|}{\sigma_r}} \right\} \quad (13)$$

$$\Omega(p) = \begin{cases} \omega_1 & : W_p > \tau_{nn} \text{ and } T_p > \tau_h \\ \omega_2 & : \text{otherwise} \end{cases} \quad (14)$$

where,  $\tilde{d}_p$  and  $\tilde{d}_q$  are the median disparities (to compensate for noise in the initial estimate) of the segments where pixels  $p$  and  $q$  come from.  $\hat{N}(p)$  is the perimeter of the segment where  $p$  comes from. Notice that eq.12 computes a value per segment, while eq.13 does it per pixel by aggregating neighboring values based on intensity similarity.  $\tau_{nn}$  is dynamically computed from  $W_p$  using Otsu threshold. Eq.14 measures the number of pixels that can be considered and edge for being above a threshold.

### 3.2 Uniqueness and out of range terms

The Similarity function described above only takes into consideration intensity to compute a matching score. However, this has the implicit assumption that each pixel has a unique match, which in general is not necessarily true (e.g.2), especially in occluded areas and textureless regions that are prone to have multiple matches (see red boxes in fig.3). Eq.15 penalizes each pixel that has multiple matches (similar to (Kolmogorov and Zabih, 2001)).

$$U(D_p) = \begin{cases} \tau_{unique} & : L(D_p) \\ 0 & : \text{otherwise} \end{cases} \quad (15)$$

where  $L(D_p)$  is true when a pixel  $p$  is mapped to  $d + D_p$  which has more than one match. This is done per hypotheses, which means it's a local uniqueness terms, unlike (Kolmogorov and Zabih, 2001) and (Vogel et al., 2015) where it's represented as part of the MRF.

A plane  $D_p$  evaluated at a different pixel  $q$  in the image could have disparity values that lie outside

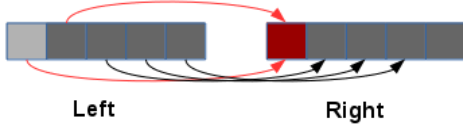


Figure 2: Example of uniqueness constraint violation; two pixels (red arrows) in left image scanline map to a single pixel in right image (red pixel).

a defined search range of disparities. Eq.16 penalizes disparity values that lie outside a defined search range.

$$O(D_p) = \begin{cases} 1 - \exp(-|D_p - \min D|/\sigma_d) & : D_p < \min D \\ 1 - \exp(-|D_p - \max D|/\sigma_d) & : D_p > \max D \\ 0 & : \text{otherwise} \end{cases} \quad (16)$$

where  $\min D$  and  $\max D$  are the minimum and maximum of the disparity search range, while  $\sigma_d$  is the maximum deviation allowed for values outside the search range. Eq.7 is updated to include eq.15 and eq.16, which then becomes:

$$\hat{C}_p(D_p) = C_p(D_p) + U(D_p) + O(D_p) \quad (17)$$

Note that the proposed uniqueness term requires to keep track of its current value after inference to update the current cost (eq.17) and prevent energy from oscillating in later iterations.

### 3.3 Search range detection

To detect spurious disparities the probability distribution (from the normalized disparity histogram) of each disparity present in both the left and right disparity maps is computed using an initial search range  $[\min D, \max D]$ , and an n-point (n is 18% of the initial disparity search range) Parzen window is applied to smooth the probability distribution.

Finally, a search finds the lowest ( $\min \hat{D}$ ) and largest disparities ( $\max \hat{D}$ ) that are above a threshold  $\tau_{\max D}$  and  $\tau_{\min D} = \frac{2}{3}\tau_{\max D}$ . It's possible that  $\min \hat{D}$  is over estimated and  $\max \hat{D}$  under estimated, which is addressed by  $\min \hat{D} = \max(\min D, \min \hat{D} - \Delta \min D)$ , and  $\max \hat{D} = \min(\max D, \max \hat{D} + \Delta \max D)$ . The estimated bounds on the disparities are used to eliminate or penalize unrealistic disparities.  $\max \hat{D}$  is used during the inference process, and  $\min \hat{D}$  during the post-processing stage.

### 3.4 Smoothness term

The assumption made by the proposed edge model is that possible depth discontinuities are allowed small variations, while areas with a similar intensity are allowed to have larger changes, by contrast in (Besse

et al., 2012; Taniai et al., 2014) the maximum variation is constant.

$$V_{pq}(D_p, D_q) = \begin{cases} w_{pq} \lambda \omega(D_p, D_q, K2) & : |F_p - F_q| < \tau_{diff} \\ w_{pq} \lambda \omega(D_p, D_q, K1) & : \text{otherwise} \end{cases} \quad (18)$$

$$w_{pq} = \left\{ \frac{1}{Z_n} e^{-|I_{ms}(p) - I_{ms}(q)|} \right\} \quad Z_n = \sum_{q \in N(p)} e^{-|I_{ms}(p) - I_{ms}(q)|} \quad (19)$$

where  $K1 < K2$ ,  $I_{ms}$  is a gray level image after applying the quick shift segmentation<sup>3</sup> (Vedaldi and Soatto, 2008; Vedaldi and Fulkerson, 2008),  $w_{pq}$  and  $\lambda$  are weights,  $F_p$  and  $F_q$  come from a local cue map  $F$ , and  $\tau_{diff}$  is a threshold, which means the growth limit of the smoothness term adapts based on the local cue map  $F$  (eq.22), while  $\omega(D_p, D_q, K)$  is given by:

$$\omega(D_p, D_q, K) = \min(|D_p(p) - D_q(p)| + |D_q(q) - D_p(q)|, K) \quad (20)$$

$F_p$  is computed using the intensity gradient of the reference image, and is used to locate possible depth discontinuities. Using the image gradient can lead to problems in areas where the gradient is noisy (e.g. image or texture is noisy). This issue can be partially addressed by filtering both the image and gradient, which can provide a two-fold advantage. First, the gray level of the reference image is filtered (eq.21) to remove potential sources of noise (e.g. noisy edges or sensor noise). Second, a filter is applied to the gradient magnitude (eq.22) to remove false edges (e.g. small letters on a wall).

$$\hat{I}_g(p) = \left\{ \frac{1}{Z} \sum_{q \in N(p)} e^{-\frac{|I_p - I_q|}{\sigma_r}} |\nabla I_g(p)| \right\} \quad Z = \sum_{q \in N(p)} e^{-\frac{|I_p - I_q|}{\sigma_r}} \quad (21)$$

$$F_p = \left\{ \frac{1}{Z} \sum_{q \in N(p)} e^{-\frac{|I_p - I_q|}{\sigma_r}} |\nabla \hat{I}_g(p)| \right\} \quad Z = \sum_{q \in N(p)} e^{-\frac{|I_p - I_q|}{\sigma_r}} \quad (22)$$

where  $I$  is the color image,  $|\nabla \hat{I}_g(q)| = |\nabla_x \hat{I}_g(q)| + |\nabla_y \hat{I}_g(q)|$ , and  $\nabla_x \hat{I}_g(q)$  and  $\nabla_y \hat{I}_g(q)$  are obtained using the Sobel gradient operator.

## 4 HYPOTHESIS GENERATION AND PROPAGATION

The model described so far makes the assumption that each pixel has associated a set of planes from which a single optimal plane assignment ( $D$ ) is found using  $TRW$ -S. The proposed hypothesis generation algorithm will give each pixel  $p$  a set  $GH_p = D_p \cup H_p \cup$

<sup>3</sup>To handle noise in the image.

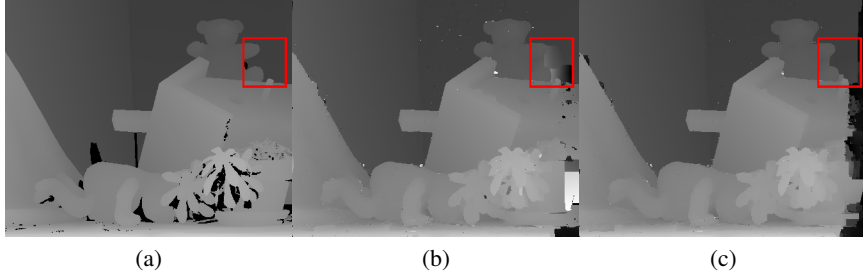


Figure 3: Raw result of Teddy image ( $\tau_{grad} = 5/255$ ,  $\tau_{cen} = 5/25$ , random initialization, and no multi-scale). (a) Groundtruth Teddy image; (b) Uniqueness term is disabled; (c) Uniqueness term is enabled.

$DS_p \cup V_p$ .  $D_p$  is the current solution,  $H_p$  is generated from pixel coordinates using ( $r$ -sampling),  $DS_p$  is generated from the pixels that belong to the same segment<sup>4</sup> ( $P$ -sampling),  $V_p$  is generated from pixels coming from another view ( $V$ -sampling). Using these disparity planes at each pixel allows the following:

1. Pixels can keep their current plane assignment  $D_p$ .
2. Pixels propagate their planes to close and distant pixels via  $r$ -sampling.
3. Segments help to propagate large disparity planes to distant pixels via  $P$ -sampling.
4. Views propagate their planes via  $V$ -sampling.

Note that hypothesis generation is done from a single disparity plane assignment  $D$  for both left and right views, and the hypothesis generation is effectively acting as a propagation scheduler once inference is done.

#### 4.1 $r$ -sampling

Algorithms that use plane propagation commonly assume that neighboring pixels are likely to have the same plane (Bleyer et al., 2011; Besse et al., 2012) or that planes are shared within a certain area (Taniai et al., 2014). The proposed  $r$ -sampling tries to generate hypotheses that are shared in a region (similar to (Taniai et al., 2014)), but also include a few planes from a distant region. The pixel coordinates used for sampling are  $(X, Y) = \{(divs * \lfloor (x+i)/divs \rfloor + r + i, divs * \lfloor (y+j)/divs \rfloor + r + j) \mid (j, i) \in [-r, r] \times [-r, r]\}$ , which come from a window of width  $2r+1$ .  $(x, y)$  are the coordinates of pixel  $p$ , and  $divs = 2r+1$ . The  $r$ -sampled plane at pixel  $p$  sampled with  $(i, j)$  is given by:

$$\hat{D}_p^{ij} = D_p^{XY} \quad (23)$$

This sampling is repeated for each  $(i, j) \in [-r, r] \times [-r, r]$  generated by a window centered at  $p$ , which

<sup>4</sup>A segment will be a set of pixels that are grouped using some logical criteria e.g. spatial distance and color similarity.

means each pixel has a set of hypotheses:

$$H_p = \bigcup_{i=-r}^r \bigcup_{j=-r}^r \hat{D}_p^{ij} \quad (24)$$

The purpose of this sampling strategy is to include the planes from all neighbors in the  $divs \times divs$  window centered at  $p$  and also neighbors that come from distant  $divs \times divs$  windows. Fig.4 shows how a  $3 \times 3$  window (i.e  $r = 1$ ) would generate several hypotheses, where each colored box is a different plane. For illustration purposes we will center our attention around the “red plane” and its eight neighbors.  $H_1 \dots H_n$  represent the hypothesis generated by using  $i$  and  $j$  according to eq.24. In particular fig.4 demonstrates how each of the non-purple planes are transformed into a hypothesis. Also note that the planes from the purple pixels are used as well (although they are not necessarily the same!). This is meant to allow the propagation of distant neighbors. This hypothesis generation strategy is similar to that of (Taniai et al., 2014), but ours does not impose a sub-modular requirement to the pairwise interaction in the generated hypothesis.

#### 4.2 $P$ -sampling

One assumption commonly used in stereo matching is that pixels with similar intensity have a similar disparity value or disparity plane. An easy way to group pixels is to use super-pixels or segments (e.g. SLIC (Achanta et al., 2012) in this paper), which are then initialized with a plane. The disparity plane  $DS_p$  is assigned to a segment  $s_p$  by randomly selecting a plane from the planes associated with the pixels that belong to the segment:

$$DS_p = D\phi(p) \quad (25)$$

$DS_p$  denotes a plane at pixel  $p$  that was assigned by function  $D\phi(p)$  which randomly selects a plane such that it belongs to the same segment as pixel  $p$ . This criteria will only generate one hypothesis per pixel, although there may be other planes in the same segment. This is done under the assumption that one

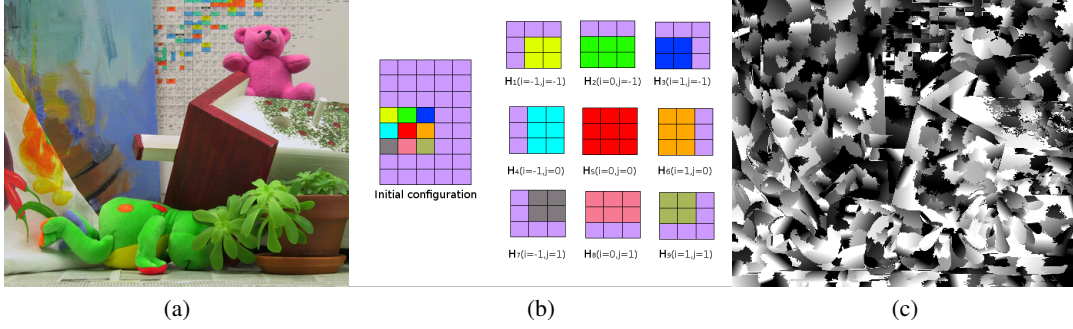


Figure 4: Hypothesis generation: (a) Teddy image; (b)  $r$ -sampling; (c)  $DS_p = D\Phi(p)$ .

of planes selected may be correct without the need of fitting one plane to the entire segment. Although each  $DS_p$  is assigned to several pixels (depending on the super-pixel algorithm used), it may be desirable to create additional hypotheses from the segments that surround  $s_p$ . To sample the neighboring segments the centroid of each  $s_p$  is computed, all neighboring  $s_q$  centroid segments are sorted by their polar angle with respect to  $s_p$ , and finally only the first  $P$  elements are selected.

$$DS_p = \left\{ DS_p \cup \left( \bigcup_{i=1}^P DS_{qi} \right) \mid \Theta(s_{q1}, s_p) < \dots < \Theta(s_{qP}, s_p) \right\} \quad (26)$$

where  $s_{qi} \in N(s_p)$  and  $\Theta(s_{qi}, s_p)$  is the function that evaluates the polar angle with respect to the centroid of  $s_p$ .

### 4.3 V-sampling

The hypotheses  $H_p$  and  $DS_p$  so far are generated from only one view. Since left and right sets of disparity planes are computed it's possible that one them contains planes which could be used to generate a better set of hypothesis. The additional set of hypotheses is computed by mapping the planes  $H_p \cup DS_p$  from the other view to the current image. This process will be referred to as  $V$ -sampling and can be expressed by  $V_p = DW_p \cup HW_p \cup DSW_p$ , where  $DW_p$  is the current solution of the other view,  $HW_p$  and  $DSW_p$  are the mapped versions of  $r$ -sampling and  $P$ -sampling hypotheses from the other view. Note that this doubles the number of hypotheses. For instance: assume two views are used, then for  $r = 2$  and  $P = 6$  the number of hypotheses generated would be 32 for one view, but after doing  $V$ -sampling the number of hypotheses would be 64. Note that (Bleyer et al., 2011) follows a similar approach (i.e. mapping the planes from one view to the other), but only generates one hypothesis.

## 5 REFINEMENT

Using the algorithms from the previous section, hypotheses are generated and a unique disparity plane is assigned to each pixel (i.e  $D_p$ ). The solution is then refined by generating a new set of hypotheses  $Gref_p = D_p \cup Href_p \cup DSref_p$  with perturbations (Bleyer et al., 2011) added to the plane parameters (normal vector  $\hat{n}_p$  and disparity  $d_p$ ), and the doing inference once again. The hypothesis refinement process is:

1. Given the current disparity map  $D_{curr}$ ,  $\Delta n_1 = \kappa$ ,  $\Delta d_1 = Sr \times \kappa$  as input.
2. For  $t = 1$  to  $s$  steps do:
  - (a) compute pixel hypothesis re-sampling ( $Href_p$ ), see sec.5.1.
  - (b) compute segment hypothesis re-sampling ( $DSref_p$ ), see sec.5.2.
  - (c) compute  $Gref_p = D_p \cup Href_p \cup DSref_p$  and obtain a new solution  $\hat{D}_{curr}$ .
  - (d) set  $D_{curr} = \hat{D}_{curr}$ ,  $\Delta n_t = \Delta n_{t-1}/2$  and  $\Delta d_t = \Delta d_{t-1}/2$ .

This means that for each pixel in the disparity map three situations can happen: a plane is propagated from a neighbor, a plane is refined and propagated from a neighbor, or a plane stays the same. Propagation is done simultaneously during the hypothesis refinement process, which happens due to the way hypotheses are generated. Also note that  $V$ -sampling is not used. To the best of our knowledge no other algorithm performs simultaneous propagation and refinement, which could have the potential to reduce the space needed to store hypotheses. The refinement process doubles the number of hypotheses. For instance: if  $r$ -sampling ( $r = 2$ ) and  $P$ -sampling ( $P = 6$ ) generate 32 hypotheses, then refinement would add 32 additional hypotheses (with perturbations added).



## 5.1 Pixel hypothesis re-sampling

To overcome local minima of the current disparity plane assignment, and obtain a refined version of  $r$ -sampling, each pixel is updated by randomly adding a perturbation selected from  $[-\Delta n_t, \Delta n_t]$  (uniform distribution) and  $[-\Delta d_t, \Delta d_t]$  (uniform distribution) which are initially set to  $\Delta n_1 = \kappa$  (the new normal vector has to be normalized) and  $\Delta d_1 = Sr \times \kappa$ , ( $Sr$  search range in disparity units), with  $\kappa = 0.2$  as recommended in (Besse et al., 2012). This process is repeated several times. After each step  $\Delta n_t$  and  $\Delta d_t$  are updated by setting them to  $\Delta n_t = \Delta n_{t-1}/2$  and  $\Delta d_t = \Delta d_{t-1}/2$ . This process generates a new set of hypotheses  $Href_p = H_p \cup Hn_p$  where  $Hn_p$  is generated using  $r$ -sampling from  $D_p$  after perturbations have been added.

## 5.2 Segment hypothesis re-sampling

Refined versions of the disparity planes image segment are obtained by creating variants of the current set of disparity planes per image segment. First, for each segment in the current image random disparity planes ( $DSr_p$ ) are generated using  $P$ -sampling and then noise is added. This generates a new set of hypotheses  $DSu_p = \Psi(DSr_p \cup DSrn_p)$ , where  $DSr_p$  was generated via  $P$ -sampling,  $DSrn_p$  is the perturbed version of  $DSr_p$ , and  $\Psi$  is a function that takes each pair of planes  $DSr_p^i$  and  $DSrn_p^i$  and returns the one whose cost locally minimizes eq.1, with respect to the current solution. This leaves  $P$  plane hypotheses per segment. Another set of hypotheses  $DSU_p$  is then generated, in which each segment  $SU_p$  has a number from  $[1..n]$ . These numbers are used as multipliers to control the random interval  $[-\Delta d_t, \Delta d_t]$ , such that  $\Delta^i d_t = i \times \Delta d_t$ . Thus each element of  $DSU_p$  is the  $\Delta^i d_t$  perturbed version of a plane generated by  $D\phi(p)$  to allow large jumps of disparity that can change an entire segment. This re-sampling produces a set of hypotheses  $DSref_p = DSu_p \cup DSU_p$ .

## 6 OVERALL DISPARITY ESTIMATION PROCESS

The disparity estimation process can now be summarized as follows:

1. Initialize solution  $Dleft$  and  $Dright$  to either a random plane per pixel or initialize from a pre-computed disparity map.
2. For  $t = 1$  to  $s$  steps do:
  - (a) Generate hypotheses  $GHleft_p$  and  $GHright_p$ , see sec.4.

- (b) Do inference and compute new solutions  $\hat{Dleft}$  and  $\hat{Dright}$ .
- (c) Refine the new solutions  $\hat{Dleft}$  and  $\hat{Dright}$ , see sec.5.
- (d) set  $Dleft = \hat{Dleft}$  and  $Dright = \hat{Dright}$ .

Random initialization is done by selecting a random uniform disparity. The normal  $\hat{n}$  is selected from the uniform distribution of a unit sphere.  $\Delta d$  and  $\Delta \hat{n}$  are selected in the same way. Fig.5 shows intermediate stages for the teddy image, using the proposed algorithm with random initialization. It can be observed that our approach is effectively propagating the planes and also minimizing eq.1. Notice that in the first propagation the outline of the underlying 3D surface can already be seen. When using a pre-computed disparity map<sup>5</sup> to initialize the current solution, the normal vectors are computed at five scales, averaging, and creating a plane per pixel by estimating the parameters of eq.2 using the normal vectors and current disparity.

Finally, the proposed algorithm is extended to multi-scale:

1. Precompute disparity maps  $Dleft_{pre}$  and  $Dright_{pre}$  (e.g. using SGM or random initialization).
2. Estimate window size from  $Dleft_{pre}$  and  $Dright_{pre}$  (if disparity map was precomputed).
3. Compute initial solution  $Dleft$  and  $Dright$  by downscaling  $Dleft_{pre}$  and  $Dright_{pre}$  to one quarter size and solving.
4. Compute updated solution at half-size by initializing with current  $Dleft$  and  $Dright$ .
5. Compute updated solution at full-size by combining  $Dleft_{pre}$  and  $Dright_{pre}$  with current  $Dleft$  and  $Dright$ . i.e compute  $GHpre_p \cup GH_p$  for left and right, then do inference to update current solutions, and update  $maxD$  (sec.3.3).
6. Compute updated solution at full-size by initializing with current  $Dleft$  and  $Dright$ .
7. Compute occlusion detection and post-processing.

The post-processing is done by computing occluded, and mismatched areas as in (Žbontar and LeCun, 2015). Then masks containing non-occluded areas, and depth edges<sup>6</sup> are eroded and marked as occluded to reduce the fattening effect. Then  $minD$  is updated (sec.3.3), and disparities lower than  $minD$  are marked as occluded. The occluded areas are then filled in using simple background interpolation and

<sup>5</sup>The pre-computed disparity map is obtained using SGM, see support material.

<sup>6</sup>detected using Canny edge detector.



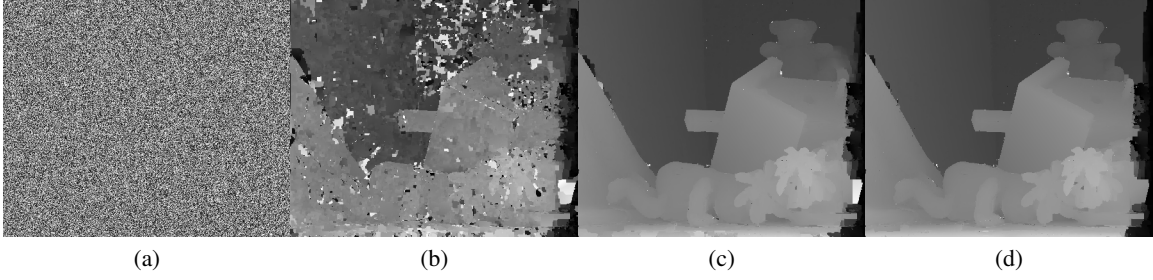


Figure 5: Proposed algorithm with random initialization ( $\tau_{grad} = 5/255$ ,  $\tau_{cen} = 5/25$ , and no multi-scale), intermediate and final results: (a) Initial random configuration; (b) First propagation,  $E = 123,257.02$ ; (c) First Refinement,  $E = 87,134.61$ ; (d) Final Result,  $E = 82,334.98$ .

filtered by applying a weighted median filter. The non-occluded areas are NOT post-processed.

All experimental results were carried out using the multi-scale approach with pre-computed initialization. The proposed algorithm uses the following parameters for all scales: aggregation window sizes of  $\omega_1 = 41 \times 41$ ,  $\omega_2 = 25 \times 25$ ,  $\tau_{grad} = 3/255$ ,  $\tau_{cen} = 9/25$ ,  $\sigma_r = 10/255$ ,  $\sigma_d = 0.5$ ,  $\tau_w = 2.5$ ,  $\tau_{diff} = 0.07$ ,  $\alpha = 30$ ,  $K_1 = 1$ ,  $K_2 = 6$ ,  $r = 2$ ,  $P = 6$ ,  $\tau_h = 2$ ,  $\tau_w = 0.5$ ,  $K_w = 8$ . For quarter and half size  $\lambda = 0.06$ , and  $\lambda = 0.12$  for full size. The disparity estimation is iterated 4 times at quarter size, 1 time at half-size and 4 times at full size. The refinement iterations are set to 5 times each scale. These parameters were obtained by using the Middlebury training data, and every fifth image from KITTI 2015 and 2012 training data.

## 7 PROPOSED APPROACH VS. STATE OF THE ART

The approach presented in this paper was validated in three stages. First, the proposed content aware adaptive windows are compared to the traditional approach, as well as the tolerance to noise and evaluation of  $r$ -sampling performance. Then the proposed algorithm is extensively validated on three data sets: The new Middlebury (15 images) data set (Scharstein et al., 2014), KITTI 2015 (Menze and Geiger, 2015) and 2012 (Geiger et al., 2012) (up to 200 images). The only parameters that are set differently are  $\Delta_{minD}$  (10 for Middlebury and 5 for KITTI),  $\Delta_{maxD}$  (60 for Middlebury and 20 for KITTI) and  $\tau_{maxD}$  (0.0028 for Middlebury and 0.0003 for KITTI).

To test the performance of the proposed similarity function three competing functions are compared (tab.1):  $AW$  is the traditional approach (eq.4) with the enabled out of range term, but no uniqueness term.  $AW + CW$  is the proposed adaptive window

Table 1: Comparative table of the proposed content aware function vs adaptive windows. Evaluation done with the Middlebury training data set at half size in non occluded areas before post-processing.

Function	%bad noc	avg. error	rms
$AW$	13.62	2.00	7.62
$AW + CW$	13.58	1.98	7.67
$AW + CW + U$	12.95	1.82	7.28

(eq.7) with the enabled out of range term, but no uniqueness term.  $AW + CW + U$  is the proposed adaptive window with the out of range and local uniqueness terms (eq.17). Our innovations (eq.17) clearly improve on the popular adaptive windows (Yoon and Kweon, 2006) commonly used in DPI algorithms.

Table 2: Evaluation of  $r$ -sampling and proposed approach (all stages enabled) tolerance to noise in initial disparity map, using every fifth image from KITTI 2015 training data.  $ns0$  no noise, and added disparity noise  $[-1, 1]$  ( $ns1$ ),  $[-2, 2]$  ( $ns2$ ),  $[-3, 3]$  ( $ns3$ ).

Algorithm	%bad D1-bg	%bad D1-fg	%bad D1-all
$ns0$	2.96	9.26	3.86
$LSL$	2.90	9.55	3.86
$ns1$	2.94	9.49	3.89
$ns2$	2.96	9.39	3.88
$ns3$	2.94	9.85	3.94

To evaluate the effectiveness of  $r$ -sampling we replace it with the pixel shared hypotheses  $LSL$  from (Taniai et al., 2014). In tab.2 our sampling strategy ( $ns0$ ) in general matches the performance of  $LSL$ , and even gives improved performance for foreground objects  $D1 - fg$ , which is caused by the larger number of hypotheses 25 for  $r$ -sampling vs. 16 for  $LSL$  due to different hypothesis generation strategies. The performance of our approach in tab.2 shows that the proposed approach  $ns0$  is robust to several levels of uni-

form real valued noise added to the initial disparity map.

The main competitors to our algorithm are *MCNCC*(Žbontar and LeCun, 2015) and *MDP*(Li et al., 2016a), since they were evaluated using the same data sets (see tab.3 and tab.4). To compare to the state of the art, from all data sets competitors were selected by choosing the best performing convolutional neural network algorithms and the best performing algorithm not using convolutional neural networks. For the KITTI 2015 and 2012 results, algorithms must appear in both data sets evaluation tables. The proposed algorithm is among top performers in the Middlebury (tab.3) and KITTI 2015/2012 (tab.4 and tab.5). In tab.3 the disparity map is evaluated only in non-occluded areas, integer and sub-pixel scores are computed using an error pixel threshold of 2.0 (rank 9<sup>th</sup> out of 44) and 0.5 (rank 8<sup>th</sup> out of 44) respectively.

Table 3: Comparative table of results (on non-occluded pixels) on the new Middlebury data set. Only non-anonymous entries are used for comparison: PMSC(Li et al., 2016b), Mesh and MeshE(Zhang et al., 2015), APAP(Park and Yoon, 2016), MCNCC(Žbontar and LeCun, 2015), MDP(Li et al., 2016a)

Algorithm	%bad > 2.0	%bad > 0.5	avg. error	rms
<i>Our</i> <sup>7</sup>	10.50 <sup>9th</sup>	43.2 <sup>8th</sup>	3.17	15.6
PMSC <sup>8</sup>	6.87 <sup>1st</sup>	39.1 <sup>1st</sup>	2.27	12.9
MeshE <sup>9</sup>	7.29 <sup>2nd</sup>	40.1 <sup>2nd</sup>	2.50	15.4
APAP <sup>10</sup>	7.46 <sup>3rd</sup>	50.9 <sup>12th</sup>	3.89	21.1
MCNCC	8.29 <sup>5th</sup>	40.7 <sup>4th</sup>	3.82	21.3
MDP	12.6 <sup>10th</sup>	61.8 <sup>27th</sup>	5.28	23.1
Mesh	13.4 <sup>11th</sup>	51.2 <sup>13th</sup>	4.63	20.1

In the KITTI benchmark, our algorithm ranks 8<sup>th</sup> (out of 38), and 14<sup>th</sup> (out of 83) for KITTI 2015 and 2012 respectively. The evaluation on KITTI 2012 proved more challenging (tab.5) mostly in the presence of reflective regions, and color image misalignment (the gray images are colored, and not properly aligned to the ground truth shape image). The top performing algorithms (for KITTI 2015 and 2012) currently achieve high performance by: exploiting scene specific content to solve ambiguities (e.g. cars in Disp.v2), training specifically for the data set (e.g. MCNCC), or using multiple image pairs to estimate disparity (e.g. PRSM, OSF). By contrast the proposed

<sup>7</sup>Submitted to both KITTI and Middlebury benchmarks as LPU.

<sup>8</sup>Unpublished work at the time of submission.

<sup>9</sup>Mesh(Zhang et al., 2015) using the cost from (Žbontar and LeCun, 2015), but not published.

<sup>10</sup>Unpublished work at the time of submission.

algorithm achieves top performing results in multiple data set by: using only one image pair, solving at different scales, not using scene specific features (e.g. cars), and generating a set of hypothesis from a single initial hypothesis.

Table 4: Comparative table of results (all pixels evaluated) on the KITTI 2015 data set. Only non-anonymous entries are used for comparison: Disp.v2(Guney and Geiger, 2015), PRSM(Vogel et al., 2015), OSF(Menze and Geiger, 2015).

Algorithm	%bad D1-bg	%bad D1-fg	%bad D1-all
<i>Our</i> <sup>8th</sup>	3.55	12.30	5.01
Disp.v2 <sup>1st</sup>	3.00	5.56	3.43
MCNCC <sup>3rd</sup>	2.89	8.88	3.89
PRSM <sup>5th</sup>	3.02	10.52	4.27
MDP <sup>12th</sup>	4.19	11.25	5.36
OSF <sup>15th</sup>	4.54	12.03	5.79

Table 5: Comparative table of results (all pixels evaluated) on the KITTI 2012(Geiger et al., 2012) data set. Only non-anonymous entries are used for comparison.

Algorithm	%bad noc	%bad occ	avg. noc	avg. occ
<i>Our</i> <sup>14th</sup>	3.22	4.27	0.80	1.00
Disp. v2 <sup>2nd</sup>	2.37	3.09	0.70	0.80
MCNCC <sup>4th</sup>	2.43	3.63	0.70	0.90
PRSM <sup>8th</sup>	2.78	3.00	0.70	0.70
OSF <sup>15th</sup>	3.28	4.07	0.80	0.90

## 8 CONCLUSIONS

The proposed algorithm delivers top performing results even though only one global hypothesis is used (eliminating the need to update multiple hypotheses), and no convolutional neural network (e.g. (Zhang et al., 2015; Žbontar and LeCun, 2015; Guney and Geiger, 2015)) or prior 3D models (e.g. cars) are used. The use of *r*-sampling and *P*-sampling are novel, simple and effective ways of simulating a propagation scheduler, which can be executed in parallel, unlike those from (Bleyer et al., 2011; Besse et al., 2012; Zhang et al., 2015). The proposed similarity function is also capable of reducing some of the loss of detail and error caused by the popular adaptive window approach.

## REFERENCES

- Achanta, R., Shaji, A., Smith, K., Lucchi, A., Fua, P., and Süsstrunk, S. (2012). Slic superpixels compared to state-of-the-art superpixel methods. *PAMI*, 34(11):2274–2282.
- Besse, F., Rother, C., Fitzgibbon, A., and Kautz, J. (2012). Pmbp: Patchmatch belief propagation for correspondence field estimation. *International Journal of Computer Vision*, 110(1):2–13.
- Bleyer, M., Rhemann, C., and Rother, C. (2011). Patchmatch stereo - stereo matching with slanted support windows. In *Proceedings of the British Machine Vision Conference*, 11:1–11.
- Geiger, A., Lenz, P., and Urtasun, R. (2012). Are we ready for autonomous driving? the kitti vision benchmark suite. *CVPR*, pages 3354–336.
- Guney, F. and Geiger, A. (2015). Displets: Resolving stereo ambiguities using object knowledge. *CVPR*.
- Heise, P., Klose, S., Jensen, B., and Knoll, A. (2013). Patchmatch with huber regularization for stereo matching. *ICCV*, pages 2360–2367.
- Klaus, A., Sormann, M., and Karner, K. (2006). Segment-based stereo matching using belief propagation and a self-adapting dissimilarity measure. *ICPR*, 3:15–18.
- Kolmogorov, V. (2007). Convergent tree-reweighted message passing for energy minimization. *IEEE Transactions on Pattern Analysis and Machine Intelligence*, 28(10):1568–1583.
- Kolmogorov, V. and Zabih, R. (2001). Computing visual correspondence with occlusions using graph cuts. *ICCV*, 2:508–515.
- Li, A., Chen, D., Liu, Y., and Yuan, Z. (2016a). Coordinating multiple disparity proposals for stereo computation. *CVPR*.
- Li, L., Zhang, S., Yu, X., and Zhang, L. (2016b). Pmsc: Patchmatch-based superpixel cut for accurate stereo matching. *IEEE Transactions on Circuits and Systems for Video Technology*.
- Li, Y., Min, D., Brown, M. S., Do, M. N., and Lu, J. (2015). Sped-up patchmatch belief propagation. *ICCV*.
- Menze, M. and Geiger, A. (2015). Object scene flow for autonomous vehicles. *CVPR*.
- Olsson, C., Ulén, J., and Boykov, Y. (2013). In defense of 3d-label stereo. *CVPR*, pages 1730–1737.
- Park, M.-G. and Yoon, K.-J. (2016). As-planar-as-possible depth map estimation. *Submitted to IEEE TPAMI*.
- Scharstein, D., Hirschmüller, H., Kitajima, Y., Krathwohl, G., Nesić, N., Wang, X., and Westling, P. (2014). High-resolution stereo datasets with subpixel-accurate ground truth. In *German Conference on Pattern Recognition (GCPR)*, pages 31–42.
- Sinha, S., Scharstein, D., and Szeliski, R. (2014). Efficient high-resolution stereo matching using local plane sweeps. *CVPR*, pages 1582–1589.
- Tanai, T., Matsushita, Y., and Naemura, T. (2014). Graph cut based continuous stereo matching using locally shared labels. *CVPR*, pages 1613–1620.
- Vedaldi, A. and Fulkerson, B. (2008). VLFeat: An open and portable library of computer vision algorithms. <http://www.vlfeat.org/>.
- Vedaldi, A. and Soatto, S. (2008). Quick shift and kernel methods for mode seeking. *ECCV*, 5305:705–718.
- Vogel, C., Schindler, K., Konrad, and Roth, S. (2015). 3d scene flow estimation with a piecewise rigid scene model. *IJCV*, pages 1–28.
- Žbontar, J. and LeCun, Y. (2015). Stereo matching by training a convolutional neural network to compare image patches. *Submitted to JMLR*.
- Woodford, O. J., Reid, I. D., Torr, P. H. S., and Fitzgibbon, A. W. (2007). On new view synthesis using multiview stereo. In *Proceedings of the British Machine Vision Conference*, pages 1–10.
- Yamaguchi, K., McAllester, D., and Urtasun, R. (2014). Efficient joint segmentation, occlusion labeling, stereo and flow estimation. *ECCV*, pages 756–771.
- Yoon, K. and Kweon, I. (2006). Adaptive support-weight approach for correspondence search. *IEEE Transactions on Pattern Analysis and Machine Intelligence*, 28(4):650–656.
- Zabih, R. and Li, J. (1994). Non-parametric local transforms for computing visual correspondence. *ECCV*, 12:151–158.
- Zhang, C., Li, Z., Cheng, Y., Cai, R., Chao, H., and Rui, Y. (2015). Meshstereo: A global stereo model with mesh alignment regularization for view interpolation. *ICCV*.
- Zhang, K., Lu, J., and Lafruit, G. (2009). Cross-based local stereo matching using orthogonal integral images. *IEEE Transactions on Circuits and Systems for Video Technology*, 19(7):1073–1079.